Discover Oncology

Research

Prognostic and therapeutic insights from lactate metabolism and tumor immune microenvironment in head and neck squamous cell carcinoma

Huanyu Jiang[1,2] · Lijuan Zhou[2] · Haidong Zhang[1,2] · Shanchun Gong[2] · Zhenkun Yu[1,2]

Received: 8 January 2025 / Accepted: 13 May 2025
Published online: 24 May 2025

Abstract

Head and neck squamous cell carcinoma (HNSCC) exhibits a poor prognosis, particularly in advanced stages characterized by high recurrence and metastasis rates. This study investigates the role of lactate metabolism in HNSCC, aiming to develop a prognostic model to predict immunotherapy outcomes. Genomic and clinical data from The Cancer Genome Atlas and Gene Expression Omnibus databases were analyzed, focusing on 233 lactate metabolism-related genes (LMGs). Differential expression and Cox regression analyses identified two significant prognostic genes: glycogen phosphorylase L (*PYGL*) and solute carrier family 16 member 3 (*SLC16 A3*, encoding MCT4). A lactate risk score (LRS) model constructed from these genes demonstrated robust predictive accuracy across multiple validation datasets. Multivariate analysis validated LRS as an independent prognostic factor, and a nomogram integrating LRS with clinical parameters further improved survival prediction accuracy. Immune infiltration analyses revealed distinct immune landscapes between high- and low-risk groups. Elevated levels of CD4 naïve T cells, resting NK cells, M0 macrophages, and activated mast cells characterized the high-risk group, whereas naive B cells, plasma cells, CD8 T cells, T follicular helper cells, regulatory T cells, gamma delta T cells, resting dendritic cells, resting mast cells, and eosinophils predominated in the low-risk group. Additionally, molecular docking suggested valproic acid as a potential inhibitor of MCT4. Immunohistochemical analyses showed increased PYGL and MCT4 expression correlated with advanced tumor stage, alongside decreased expression of CXCL9 and CXCL10. These findings highlight the critical role of lactate metabolism in HNSCC progression and immunotherapy resistance, identifying PYGL and MCT4 as promising therapeutic targets.

Keywords Head and neck squamous cell carcinoma · Immunotherapy · Lactate metabolism · Prognosis · Tumor immune microenvironment

Supplementary Information The online version contains supplementary material available at https://doi.org/10.1007/s12672-025-02706-w.

✉ Zhenkun Yu, yuzhenkun65@hotmail.com | [1]School of Medicine, Southeast University, 87 Dingjiaqiao, Hunan Road, Nanjing 210009, Jiangsu, China. [2]Department of Otolaryngology Head and Neck Surgery, The Affiliated BenQ Hospital of Nanjing Medical University, Nanjing 210019, Jiangsu, China.

1 Introduction

Head and neck squamous cell carcinoma (HNSCC), ranking as the sixth most common cancer globally, is often identified at an advanced stage, resulting in a poor prognosis [1]. The global annual incidence of HNSCC is approximately 5.4 per 100,000 individuals, with a mortality rate of 2.9 per 100,000 [2]. Key risk factors that significantly elevate the incidence of this disease include smoking, alcohol consumption, and human papillomavirus infection. Clinically, HNSCC is characterized by aggressive local invasiveness, a high propensity for metastasis, and unfavorable outcomes [3, 4].

Despite recent advancements in treatment strategies, the prognosis for HNSCC remains dismal, particularly for patients in advanced stages who experience high rates of recurrence and metastasis [5]. Immunotherapy has rapidly evolved as a treatment modality for HNSCC, with immune checkpoint inhibitors (ICIs) representing a significant breakthrough, especially in recurrent or metastatic cases. The intricate immune evasion strategies of HNSCC and the significant impact of the tumor immune microenvironment (TME) lead to sustained immunotherapy responses in only a small subset of patients [6]. Therefore, it is crucial to improve immunotherapy outcomes by altering the metabolic conditions within the TME.

Tumor cells frequently enhance glycolytic pathways, resulting in significant lactate production even under oxygen-rich conditions, which raises lactate levels in the TME [7]. Elevated lactate promotes tumor growth and impairs immune cell function by modifying the TME, thereby aiding in immune evasion [8]. Understanding lactate metabolism in HNSCC, particularly its impact on the TME, is essential for developing novel therapeutic strategies.

Although lactate metabolism is well documented in various cancers, comprehensive investigations in HNSCC are still lacking. In particular, the roles and mechanisms of lactate (LA) in HNSCC progression remain poorly understood. To address this gap, we used bioinformatics to identify lactate metabolism-related genes (LMGs) and developed a lactate risk score (LRS) signature for prognostic stratification. Correlation analyses and functional enrichment were performed to elucidate the biological roles of the signature genes within the TME. Molecular docking and dynamics simulations were employed to evaluate interactions between candidate small-molecule drugs and key target proteins. These findings may provide novel insights into targeted therapeutic strategies for HNSCC.

2 Materials and methods

2.1 Data acquisition and processing

Genomic and clinical data for 546 HNSCC samples were sourced from The Cancer Genome Atlas (TCGA-HNSC) through the UCSC Xena database [9]. This dataset includes 502 HNSCC samples and 44 normal control samples, with survival data available for 494 patients. The detailed clinical characteristics are summarized in Supplementary Table S1. Additionally, the R package GEOquery [10] was utilized to retrieve the HNSCC datasets GSE65858 [11] and GSE27020 [12] from the Gene Expression Omnibus (GEO) database. The GSE65858 dataset, based on the GPL10558 microarray platform, comprises 253 primary tumor samples, while the GSE27020 dataset, based on the GPL96 microarray platform, includes 109 tumor samples. A total of 314 LMGs were retrieved from the MSigDB database [13], and 233 genes present across all three datasets were retained for subsequent analyses.

2.2 Differential expression analysis

TCGA-HNSC samples were categorized into HNSCC and normal groups. Differential expression analysis was performed using the R package limma (v3.58.1), identifying significant differences with $|\log_2 FC| \geq 1$ and an adjusted P-value < 0.05. Differentially expressed LMGs were visualized using the R packages ggplot2 and pheatmap to generate volcano plots and heatmaps.

2.3 Mutation and copy number variation analysis

Somatic mutation data in the form of a VarScan MAF file for TCGA-HNSC were downloaded and analyzed using the R package maftools (version 2.18.0) [14]. The 30 LMGs with the highest mutation frequencies were visualized using waterfall plots. Kaplan–Meier survival analysis was conducted to compare outcomes between patients with mutated versus

wild-type LMGs. Copy number variation (CNV) data were processed using GISTIC 2.0 (Broad Institute, Cambridge, MA, USA). CNV statuses were classified as gain (1), loss (– 1), or no change (0), and the top 30 LMGs with CNV alterations were visualized via heatmaps.

2.4 Construction and validation of the prognostic model

The coxph function from the R package survival was utilized to conduct univariate Cox regression analysis on differentially expressed LMGs, aiming to identify prognostically relevant genes. Genes with *P*-value below 0.05 were deemed prognostic and chosen for additional analysis. The LRS model was constructed by applying least absolute shrinkage and selection operator (LASSO) regression to the prognostic LMGs using the R package glmnet [15]. The risk score for each sample was determined using the prognostic LMGs and their coefficients derived from LASSO regression, applying the formula: Risk score = ∑(exp(i) × coef(i)), where (i) represents a gene, exp(i) is the gene expression level, and coef(i) is the LASSO coefficient for the corresponding gene.

Samples were stratified into high- and low-risk groups based on the median risk score. Survival scatter plots and Kaplan–Meier survival curves illustrating prognostic differences between the two groups were generated using the R packages ggplot2, survminer, and survival [16]. The predictive accuracy of the model was evaluated using receiver operating characteristic (ROC) curves generated with the survivalROC package. Heatmaps displaying the expression of prognostic LMGs in high- and low-risk groups were created using the pheatmap package. To confirm the robustness and predictive capability of the model, external validation was performed with the independent datasets GSE65858 and GSE27020.

2.5 Association of LRS with clinical characteristics

To assess the independence and clinical utility of the LRS model, multivariate Cox regression analysis was conducted including clinical parameters such as age, sex, grade, TNM stage, alcohol consumption, and peripheral nerve invasion (PNI). The results were visualized using forest plots (via the forestplot package). A nomogram integrating LRS, age, and N stage was constructed using the rms package to predict 1-, 2-, and 3-year survival. Calibration curves were used to evaluate the predictive performance of the nomogram.

2.6 Immune cell infiltration and immune checkpoint analysis

The CIBERSORT method [17] was used to examine differences in immune cell infiltration and immune checkpoint gene expression between high- and low-risk groups. Normalized TCGA-HNSC expression data were uploaded to the CIBERSORTx platform. The algorithm utilized the LM22 signature matrix to perform 100 permutations, estimating the relative abundance of 22 immune cell types, including macrophages, T cells, NK cells, mast cells, B cells, dendritic cells, monocytes, plasma cells, neutrophils, and eosinophils. The Wilcoxon rank-sum test assessed immune cell infiltration differences between groups, considering $P < 0.05$ as significant. Boxplots were used to compare immune checkpoint gene expression (CD274, PDCD1LG2, CTLA4, CD80, CD86) between the two groups.

2.7 Immunotherapy response prediction

To evaluate the predictive value of LRS for immunotherapy outcomes, the GSE78220 dataset [18], which includes data from 28 melanoma patients treated with anti-PD-1 therapy, was analyzed. Samples with incomplete survival data were excluded. LRS was calculated and compared between responders and non-responders.

2.8 Correlation analysis of LRS with cancer hallmark pathways

Single-sample Gene Set Enrichment Analysis (ssGSEA) was conducted using the GSVA package with hallmark gene sets from MSigDB. Pearson correlation analysis was used to assess associations between LRS and pathway enrichment scores, with significance set at $P < 0.05$ and $|R| > 0.2$.

2.9 Construction of regulatory networks

Protein–protein interaction (PPI) networks for *PYGL* and *SLC16 A3* were constructed using the STRING database [19] (interaction score ≥ 0.4). Competing endogenous RNA (ceRNA) networks involving miRNAs and lncRNAs were built using data from StarBase v3.0 [20]. Transcription factor (TF) interactions were predicted via ChIPBase [21], and RNA-binding protein (RBP) interactions were identified using StarBase. Drug-gene interactions were retrieved from the Comparative Toxicogenomics Database (CTD) [22]. All networks were visualized using Cytoscape [23].

2.10 Molecular docking and molecular dynamics (MD) simulation

Molecular docking was conducted to evaluate interactions between target proteins and small molecules retrieved from the CTD database. Protein structures in PDB format were downloaded from the UniProt database [24] and preprocessed using PyMOL (version 2.4.0) by removing water molecules and adding hydrogen atoms to complete the structures. The 3D conformations of small molecules were obtained from the PubChem database [25]. Docking simulations were performed using HEX 8.0.0, and the results were visualized and analyzed with PyMOL to assess protein–ligand interactions.

The stability and dynamic behavior of protein–ligand complexes were further assessed through MD simulations using GROMACS 2019.6 [26]. Proteins were parameterized with the amber99 sb-ildn force field, while ligands were processed using the general Amber force field (GAFF). Each system was placed in a cubic simulation box with at least 1.0 nm between the protein and the box boundary. The system was solvated using SPC216 water molecules and neutralized by adding appropriate Na^+ and Cl^- counterions. Energy minimization was performed using the steepest descent algorithm to eliminate steric clashes and optimize geometry.

Equilibration was conducted in two phases: a constant volume and temperature (NVT) ensemble at 300 K, followed by a constant pressure and temperature (NPT) ensemble at 1 bar, each for 100 ps. Subsequently, a 100 ns production run was carried out under periodic boundary conditions. Temperature and pressure were maintained at 300 K and 1 bar using the V-rescale and Parrinello–Rahman coupling methods, respectively [27]. The equations of motion were integrated using the leapfrog algorithm with a 2 fs time step. Long-range electrostatic interactions were calculated using the Particle Mesh Ewald (PME) method [28] with a Fourier spacing of 0.16 nm. Bond constraints were applied using the LINCS algorithm [29].

Trajectory visualization, structural analysis, and animation were performed using VMD 1.9.3 and PyMOL 2.4.1 [30]. Binding free energy calculations were conducted using the gmx_mmpbsa tool (http://jerkwin.github.io/gmxtool).

2.11 Immunohistochemical analysis

This retrospective study included 47 HNSCC tissue samples and 35 adjacent normal tissue samples obtained from patients who underwent surgical treatment at the Department of Otolaryngology–Head and Neck Surgery, BenQ Medical Center, Nanjing Medical University. Ethical approval for this study was obtained from the Ethics Committee of BenQ Medical Center, affiliated with Nanjing Medical University (Approval number: 2020041401). All experiments involving human participants and clinical specimens were performed in accordance with relevant institutional guidelines and regulations. Baseline clinical characteristics of the enrolled patients are summarized in Table 1.

The tissues were fixed in 10% neutral formalin, embedded in paraffin, sectioned at 4 μm thickness, and baked at 65 °C for 2 h. Slides were then deparaffinized twice in xylene (5 min each), rehydrated through a graded ethanol series (100%, 95%, 85%, 70%; each for 5 min), and washed with PBS. Antigen retrieval was performed using citrate buffer (pH 6.0) via microwave heating at medium–high power for 10 min, followed by cooling to room temperature under running water.

Endogenous peroxidase activity was blocked with 3% H_2O_2 in methanol for 10 min, and nonspecific binding was reduced by incubating sections in 1% BSA for 20 min. Subsequently, slides were incubated overnight at 4 °C with primary antibodies: Rabbit anti-MCT4 (1:4000, 22787-1-AP, Wuhan Sanying, China), Rabbit anti-PYGL (1:400, DF12134, Affinity Biosciences, China), Rabbit anti-CXCL9 (1:400, DF9920, Affinity Biosciences, China), and Rabbit anti-CXCL10 (1:400, DF6417, Affinity Biosciences, China).

The MaxVision™ HRP Polymer secondary antibody kit (rabbit/mouse, ready-to-use, KIT-5010, Maixin Biotech, Fuzhou, China) was used at room temperature (26 °C) for 30 min. Slides were washed with PBS and stained using freshly prepared DAB chromogen. Counterstaining was performed with hematoxylin for 10 min, with differentiation using 0.1% hydrochloric

Table 1 Baseline characteristics of patients with head and neck squamous cell carcinoma

Characteristics	Overall	Percentage
Age, mean ± SD	67.745 ± 8.6815	
≥ 60	39	83.0
< 60	8	17.0
Pathological differentiation grade, n (%)		
G1	14	29.8
G2	26	55.3
G3	7	14.9
T classification, n (%)		
Tis	3	6.4
T1	11	23.4
T2	11	23.4
T3	11	23.4
T4	11	23.4
N classification, n (%)		
N0	32	68.1
N1	1	2.1
N2	11	23.4
N3	2	4.3
N4	1	2.1
Clinical stage, n (%)		
Stage 0	3	6.4
Stage I	9	19.1
Stage II	9	19.1
Stage III	8	17.0
Stage IV	18	38.3

acid alcohol solution if overstaining occurred. Finally, slides were dehydrated through an ethanol gradient, cleared in xylene (10 min twice), and mounted with neutral resin.

Positive controls included human prostate tissue (MCT4), human kidney tissue (PYGL), human prostate cancer tissue (CXCL9), and human nasopharyngeal carcinoma tissue (CXCL10). Negative controls were prepared by replacing the primary antibody with PBS. Slides were scanned using a VS200 digital pathology slide scanner (Olympus, Japan) for high-resolution imaging.

3 Results

3.1 Expression and mutation landscape of LMGs in HNSCC

A total of 233 LMGs were analyzed for differential expression between 44 normal and 546 tumor tissues. Seven genes (*SLC16 A3*, *PYGL*, *USP18*, *SPP1*, *TYMP*, *SLC16 A1*, and *COL4 A1*) were significantly upregulated in tumor tissues, while four genes (*GATM*, *SLC25 A4*, *LDHD*, and *SLC16 A7*) showed higher expression in normal tissues (Fig. 1A, B).

The most frequently mutated LMGs included *TP53*, *CFH*, *RB1*, *ASXL1*, and *PHKA2* (Fig. 1C). Samples were categorized as mutated if at least one LMG carried a mutation. Kaplan–Meier survival analysis demonstrated differences in overall survival between wild-type and mutant LMG profiles (Fig. 1D). Additionally, the six LMGs with the highest CNV frequencies were *DNAJC19*, *PC*, *NDUFV1*, *NDUFS8*, *GFM1*, and *NDUFA10* (Fig. 1E, F).

3.2 Prognostic LMG identification and construction of the LRS Model

Univariate Cox regression of the 11 differentially expressed LMGs identified *SLC16 A3* and *PYGL* as significant prognostic factors ($P < 0.05$; Fig. 2A). These genes were incorporated into a LRS model using LASSO regression (Supplementary Fig. S1). The risk score was calculated as follows:

Fig. 1 Differential expression and mutations of lactic acid metabolism-related genes (LMGs) in head and neck squamous cell carcinoma. **A** ▶ Volcano plot of differentially expressed LMGs. **B** Heat map of differentially expressed LMGs. **C** Waterfall plot of the top 30 LMGs based on mutation frequency. **D** Kaplan–Meier survival curve for wild vs. mutation samples. **E** Heatmap and **F** bar chart of the top 30 LMGs based on the copy number variation

$$\text{Risk score} = \exp(SLC16A3) \times 0.202 + \exp(PYGL) \times 0.196.$$

Patients were stratified into high- and low-risk groups based on the median LRS. Kaplan–Meier analysis in the TCGA cohort revealed a significantly poorer survival in the high-risk group ($P = 0.002$), with AUCs of 0.637, 0.624, and 0.634 for 1-, 2-, and 3-year survival, respectively (Fig. 2B). External validation using the GSE65858 cohort demonstrated significant survival stratification ($P = 0.012$), which was further confirmed in the independent GSE27020 cohort ($P = 0.031$). In the GSE65858 cohort, the AUC values were 0.699 at 1 year, 0.621 at 2 years, and 0.616 at 3 years. In the GSE27020 cohort, the corresponding AUC values were 0.703, 0.578, and 0.568, respectively (Fig. 2C, D).

3.3 Correlation between LRS and clinical features

Multivariate Cox regression analysis, incorporating clinical variables such as age, sex, grade, overall stage, T stage, and N stage, confirmed the LRS as an independent prognostic factor for HNSCC (Fig. 3A). Notably, the LRS was significantly associated with both T stage and PNI (Fig. 3B). To enhance individualized survival prediction, a nomogram was constructed by integrating the LRS, age, and N stage (Fig. 3C). This model exhibited robust prognostic performance, as evidenced by the ROC curves (Fig. 3D), and showed good calibration for 1-, 2-, and 3-year survival probabilities (Fig. 3E–G).

3.4 Immunohistochemical expression of PYGL, MCT4, CXCL9, and CXCL10 in HNSCC

Immunohistochemical staining revealed a progressive increase in PYGL and MCT4 protein expression with advancing clinical stages of HNSCC. Quantification based on integrated optical density (IOD) confirmed significantly elevated expression levels of both proteins from stage 0 to stage IV ($P < 0.01$), as shown in Fig. 4. Representative images of PYGL (Fig. 4A) and MCT4 (Fig. 4B) expression in tumor tissues versus adjacent normal tissues are presented. Supplementary Figs. S2 and S3 provide the positive and negative controls for MCT4 and PYGL immunostaining, respectively.

In contrast, CXCL9 and CXCL10 expression exhibited a progressive decrease with advancing clinical stages of HNSCC. Quantification based on IOD confirmed significantly reduced expression levels of both markers from stage 0 to stage IV ($P < 0.01$), as shown in Fig. 5. Representative images of CXCL9 (Fig. 5A) and CXCL10 (Fig. 5B) immunostaining across different tumor stages are presented. Supplementary Figs. S4 and S5 provide the positive and negative controls for CXCL9 and CXCL10 immunostaining, respectively.

3.5 Immune cell infiltration, immune checkpoints, and immunotherapy prognosis prediction based on LRS

Using the CIBERSORT algorithm, we estimated the relative abundance of 22 tumor-infiltrating immune cell types in the training cohort. Significant differences in immune cell infiltration patterns were observed between the high-risk and low-risk groups defined by the LRS (Fig. 6A). The high-risk group exhibited increased proportions of $CD4^+$ naïve T cells, resting natural killer (NK) cells, M0 macrophages, and activated mast cells ($P < 0.05$). In contrast, the low-risk group showed higher infiltration of naive B cells, plasma cells, $CD8^+$ T cells, T follicular helper cells, regulatory T cells (Tregs), gamma delta T cells, resting dendritic cells, resting mast cells, and eosinophils ($P < 0.05$).

Among immune checkpoint molecules, CTLA4 expression was significantly upregulated in the low-risk group (Fig. 6B). Furthermore, analysis of the GSE78220 dataset revealed that patients in the low-risk group demonstrated more favorable responses to immunotherapy, with LRS showing a significant association with treatment outcomes (Fig. 6C).

3.6 Correlation analysis between LRS and cancer hallmark pathways

A correlation heatmap was used to display the 13 significantly correlated hallmark cancer pathways (Fig. 7), which positively correlated with the LRS. The five pathways exhibiting the strongest correlation were hallmark_glycolysis, hallmark_hypoxia, hallmark_p53_pathway, hallmark_tnfa_signaling_via_Nfkb, and hallmark_coagulation.

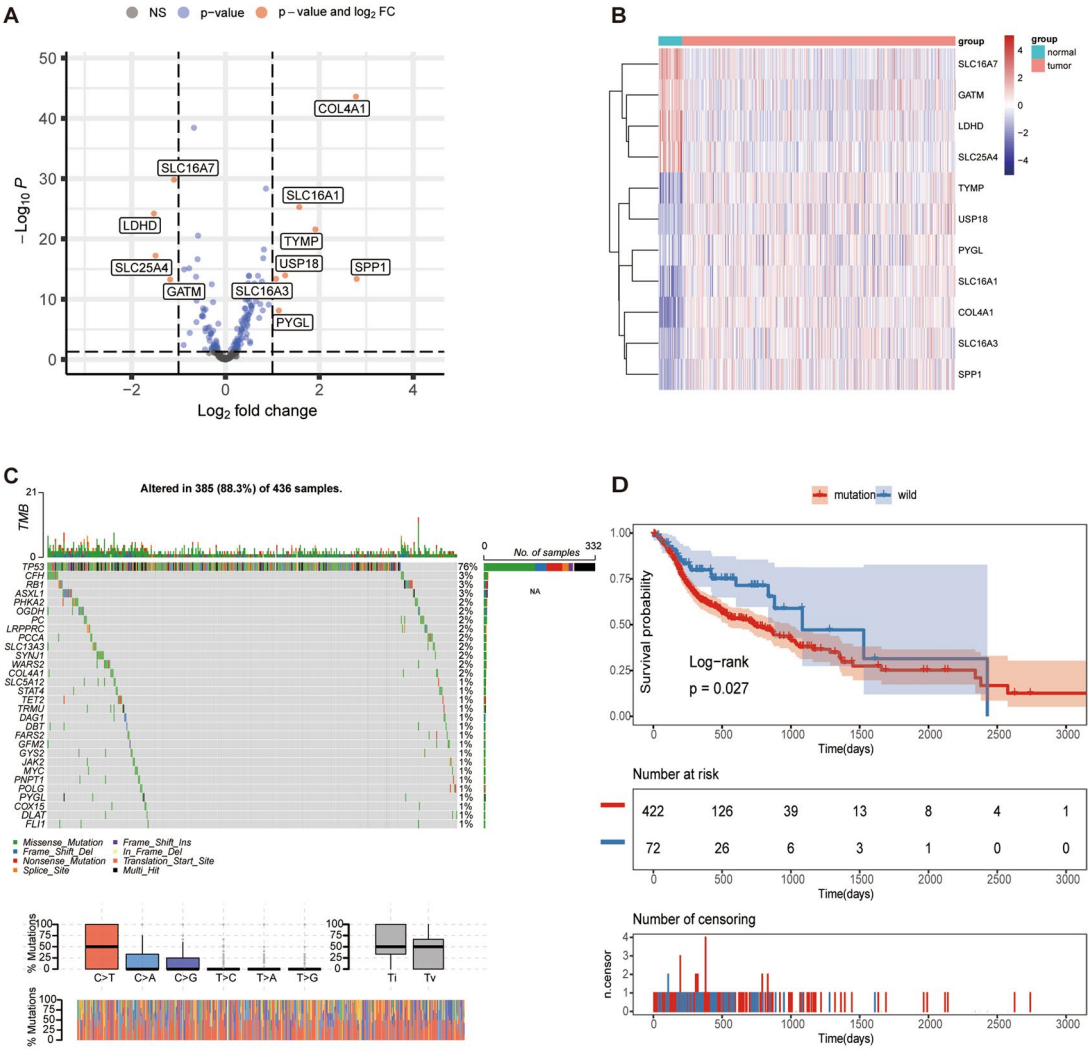
A
NS
p-value
p - value and log2 FC
−Log10 P
Log2 fold change
COL4A1
SLC16A7
SLC16A1
LDHD
TYMP
USP18
SPP1
SLC25A4
GATM
SLC16A3
PYGL
B
group
normal
tumor
SLC16A7
GATM
LDHD
SLC25A4
TYMP
USP18
PYGL
SLC16A1
COL4A1
SLC16A3
SPP1
C
Altered in 385 (88.3%) of 436 samples.
TMB
No. of samples
Missense_Mutation
Frame_Shift_Del
Nonsense_Mutation
Splice_Site
Frame_Shift_Ins
In_Frame_Del
Translation_Start_Site
Multi_Hit
% Mutations
C>T
C>A
C>G
T>C
T>A
T>G
Ti
Tv
D
mutation
wild
Survival probability
Log−rank
p = 0.027
Time(days)
Number at risk
422 126 39 13 8 4 1
72 26 6 3 1 0 0
Number of censoring
n.censor
E
NDUFB3
NDUFS1
NDUFA10
PER2
SLC19A3
MRPL44
BCS1L
PNKD
MIPEP
AGK
TPK1
FLI1
DLAT
CBL
SLC37A4
SLC7A7
SLC16A1
WARS2
NARS2
COX8A
PC
NDUFS8
NDUFV1
CYC1
MYC
NDUFB9
MRPS22
PCCB
DNAJC19
GFM1
F
gain
loss
none
CYC1
MIPEP
FLI1
DLAT
SLC37A4
PCCB
CBL
SLC16A1
NDUFB9
NDUFB3
MRPS22
SLC7A7
NARS2
WARS2
MYC
AGK
NDUFS1
TPK1
SLC19A3
PER2
PNKD
COX8A
BCS1L
MRPL44
NDUFA10
GFM1
NDUFS8
NDUFV1
PC
DNAJC19

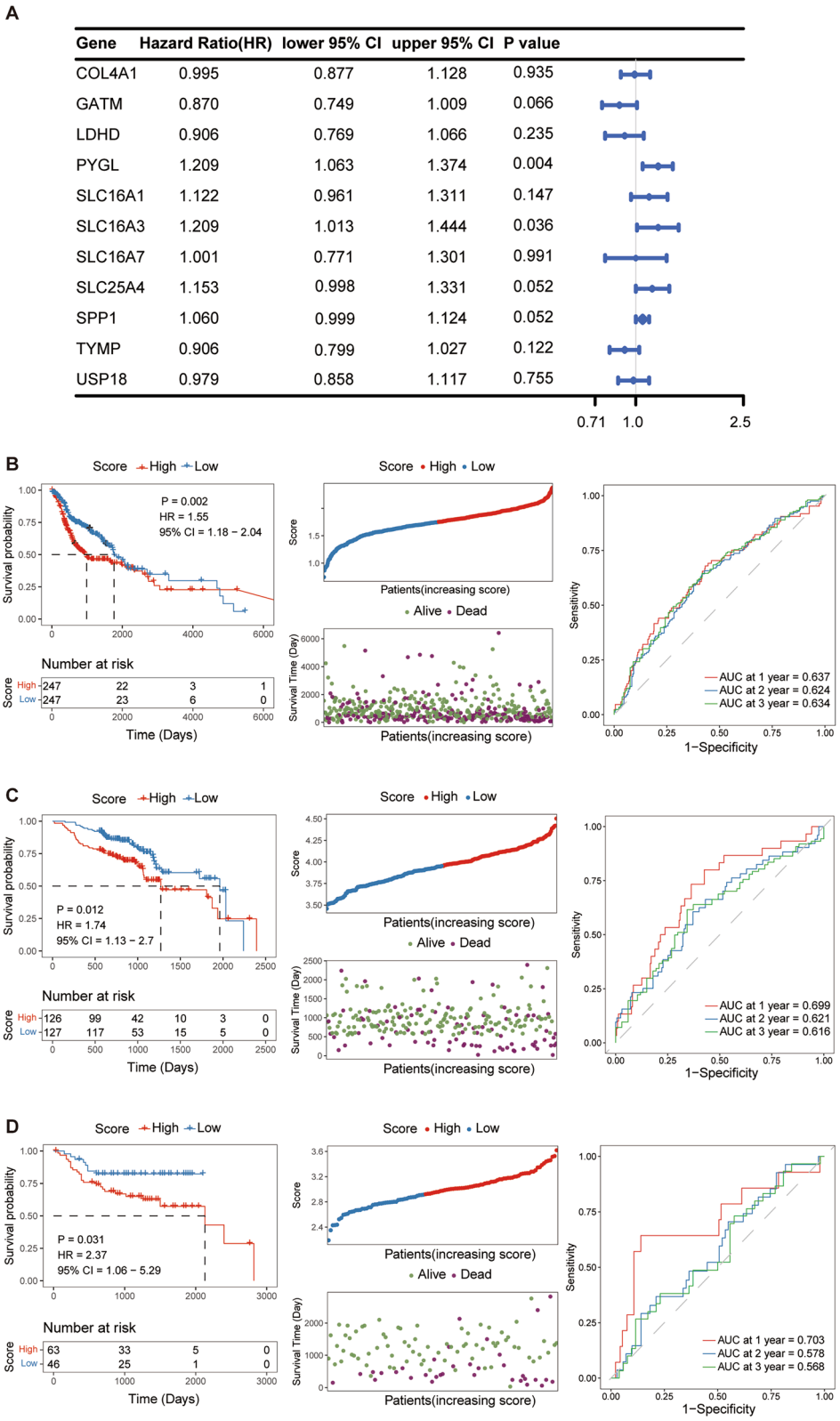

Fig. 2 Construction of the lactic acid metabolism-related prognostic signature. **A** Univariate Cox analyses of differentially expressed lactic acid metabolism-related genes (forest plot). **B** The lactic acid risk score (LRS) distribution (ranked dot plot), patient survival status (scatter plot), and Kaplan–Meier (K–M) survival curves with area under the curve (AUC) values in the training set (TCGA-HNSC). **C**, **D** The LRS distribution (ranked dot plot), patient survival status (scatter plot), and K–M survival curves with AUC values in the **C** first (GSE65858) and **D** second (GSE27020) validation sets

3.7 Protein–protein interaction (PPI) networks

The *PYGL* network included 10 interacting genes, such as *RIPK3*, *GYS2*, *GBE1*, *PYGB*, *UGP2*, *AMY1B*, *AMY2B*, *AMY2 A*, *AGL*, *MGAM* (Fig. 8A). The *SLC16 A3* network revealed interactions with 10 genes, including *LDHA*, *EMB*, *CD44*, *CBLL1*, *CA9*, *BSG*, *SLC2 A3*, *SLC2 A1*, *SLC17 A5*, *SLC16 A7* (Fig. 8B).

3.8 Regulatory network construction

Regulatory networks were constructed to elucidate potential upstream and downstream interactions of key lactate metabolism genes. Using the StarBase database, ceRNA networks were established, identifying 9 miRNAs and 11 lncRNAs associated with *PYGL* (Fig. 9A), and 9 miRNAs and 18 lncRNAs associated with *SLC16 A3* (Fig. 10A).

TF–mRNA interaction networks were constructed based on ChIPBase data, revealing 17 TFs targeting *PYGL* (Fig. 9B) and 13 TFs targeting *SLC16 A3* (Fig. 10B). In addition, mRNA–RBP interaction networks predicted through StarBase identified 10 RBPs for *PYGL* (Fig. 9C) and 24 RBPs for *SLC16 A3* (Fig. 10C).

Furthermore, chemical–gene interaction networks were derived from the CTD, identifying four chemical compounds (ethylene dichloride, tetrachlorodibenzodioxin, carbon tetrachloride, and dietary fats) interacting with *PYGL* (Fig. 9D), and five compounds (cobaltous chloride, methylmercuric chloride, nickel, oxygen, and valproic acid) interacting with *SLC16 A3* (Fig. 10D).

3.9 Molecular docking and MD simulation

Molecular docking studies indicated that MCT4 interacts with valproic acid, exhibiting a binding energy of – 166.89 kcal/mol and establishing stable hydrogen bonds with the residues ALA355 and ILE356 (Fig. 11A). Subsequent MD simulations confirmed the stability of the MCT4–valproic acid complex. The root mean square deviation (RMSD) trajectory showed that the system reached equilibrium after 10 ns, indicating a stable protein–ligand interaction (Fig. 11B). A plateau in RMSD values supports the structural stability of the complex throughout the simulation period. Solvent-accessible surface area (SASA) analysis demonstrated a gradual decline, indicating increased protein compactness over time (Fig. 11C). Similarly, the radius of gyration (Rg), which reflects the overall compactness of the protein structure, also showed a decreasing trend (Fig. 11D). Finally, the root mean square fluctuation (RMSF) analysis revealed an average value of 0.2046 nm (Fig. 11E), suggesting limited flexibility of the binding interface and further supporting the robustness of the MCT4–valproic acid interaction.

We calculated the binding energies of the protein–ligand complexes during the equilibrium phase using the gmx_mmpbsa script. As shown in Table 2, the binding free energy of the protein-Valproic Acid complex was – 51.118 kJ/mol, indicating stable binding predominantly driven by van der Waals interactions.

4 Discussion

This study systematically analyzed LMGs in HNSCC, including expression profiles, genetic alterations, prognostic significance, and associations with immune cell infiltration and checkpoint gene expression. Based on these findings, we developed a LRS model and validated its ability to predict patient prognosis and immunotherapy response. Regulatory analyses of key genes *PYGL* and *SLC16 A3* revealed potential ceRNA networks and drug interactions, while molecular docking suggested valproic acid as a potential therapeutic agent targeting MCT4, offering theoretical support for drug development. These results provide insight into the role of LMGs in HNSCC and their relevance to personalized therapy.

The LRS model achieved an AUC of approximately 0.6–0.7, reflecting reasonable prognostic performance. In comparison, Zhang et al. [31] reported an immune-related gene pair model with AUC > 0.65, and Tian et al. [32] developed a prognostic model based on cancer-associated fibroblasts, achieving AUCs of 0.67, 0.70, and 0.65 for 1-, 3-, and 5-year survival, respectively. Validation in independent datasets confirmed comparable performance (AUCs: 0.633, 0.614, 0.549). Our model thus demonstrates similar predictive reliability and practical clinical value despite not reaching the ideal AUC > 0.8.

Fig. 3 Correlation between the lactate metabolism-related prognostic signature and clinical characteristics. **A** Multivariate Cox regression analysis presented as a forest plot. **B** Association between the lactate-related risk score (LRS) and T stage, as well as PNI. **C** Nomogram incorporating the LRS, age, and N stage to predict 1-, 2-, and 3-year OS. **D** Receiver operating characteristic curves used to evaluate the predictive performance of the nomogram. **E**–**G** Calibration curves assessing the agreement between predicted and observed 1-, 2-, and 3-year OS probabilities. *PNI* perineural invasion, *OS* overall survival

PNI is a frequent invasive pattern in solid tumors, including HNSCC. Recent studies [33] show that PNI correlates with an immunosuppressive TME through neuroinflammatory interactions and altered immune infiltration, often with increased PD-L1 expression. Notably, tumors with high LRS exhibit lactate accumulation and hypoxia, which promote M2 polarization of tumor-associated macrophages and enhance tumor neuroinvasiveness via IL-6 and other mediators [34]. PNI may therefore serve as a surrogate marker of lactate-driven immune suppression and poor prognosis in high-risk LRS tumors, supporting its role as an immune-related biomarker.

High LRS was significantly associated with activation of glycolysis, hypoxia, p53, TNF-α/NF-κB, and coagulation pathways. Lactate enhances NF-κB activation via HIF-1α, promoting pro-inflammatory cytokine production and immune evasion [35, 36]. This indicates that lactate metabolism contributes to a positive feedback loop that amplifies inflammation and immune escape, thereby exacerbating tumor progression in HNSCC. Similarly, the association with the coagulation pathway suggests that lactate metabolism may influence angiogenesis and metastasis in tumors.

Analysis of immune cell infiltration revealed significant differences between high- and low-risk groups. The high-risk group showed higher levels of naïve $CD4^+$ T cells, resting NK cells, M0 macrophages, and activated mast cells, whereas Tregs were more abundant in the low-risk group. Increased resting NK cells in the high-risk group may indicate compromised immune surveillance, as NK cell activation is crucial for tumor elimination. M0 macrophages, which can differentiate into tumor-promoting M2 macrophages, were more prevalent in the high-risk group, potentially supporting tumor progression and immune suppression [37]. These findings align with evidence suggesting lactate skews macrophage polarization towards M2, fostering an immunosuppressive TME [38]. Moreover, lactate inhibits T cell function by disrupting metabolic pathways, reducing T cell activation, and impairing anti-tumor immunity [39].

CXCL9 and CXCL10 expression progressively declined with advancing HNSCC stage, suggesting impaired T cell recruitment and immune evasion. A previous study [40] showed that high expression of CXCL9 and CXCL10 is predictive of ICI responsiveness. In the same study, Liu et al. developed a model incorporating CXCL9/CXCL10, which achieved an AUC of approximately 0.75 for predicting PD-1/PD-L1 inhibitor responses in HNSCC. These findings highlight the importance of CXCL9/CXCL10 in immune surveillance and highlight their relevance in LRS-associated immune escape.

The LRS correlated with increased expression of immune checkpoint genes such as *CTLA4*, supporting earlier reports that lactate upregulates checkpoint expression via NF-κB and HIF-1α [41]. While the LRS may help predict partial responses to ICIs, its limited capacity to identify complete responders suggests that combining lactate-targeted therapies with ICIs may enhance treatment outcomes.

Mutation analysis highlighted the critical role of LMGs in HNSCC. *TP53* was the most commonly mutated gene, with its mutations known to increase glycolysis and lactate production, leading to higher lactate levels in the TME [42, 43]. This facilitates both tumor cell proliferation and immune evasion. Additionally, CNV analysis revealed that *DNAJC19* exhibited the highest CNV frequency among LMGs. As a molecular chaperone, *DNAJC19* may play an essential role in lactate metabolism, although its precise mechanisms remain poorly understood. Although *TP53* and *DNAJC19* exhibit high mutation and CNV frequencies, their expression levels do not significantly differ between tumor and normal tissues. This may be attributed to the fact that *TP53* mutations primarily exert their effects through loss of function and subsequent regulation of downstream target genes, indirectly contributing to tumor progression and lactate metabolism without altering TP53 expression levels. Similarly, *DNAJC19* CNV may regulate gene expression or influence downstream signaling pathways, indirectly affecting lactate metabolism and tumor biology. The results indicate that mutations and CNVs have intricate and diverse impacts on gene expression. Future research should explore how these genetic alterations influence lactate metabolism pathways and their potential roles in tumor biology and clinical prognosis. Integrating mutation, CNVs, and gene expression data will enable a more comprehensive understanding of these genes in HNSCC and provide new insights for targeted therapy and personalized medicine.

Molecular docking and dynamics simulations revealed high stability in the interaction between MCT4 and valproic acid, with binding free energy analyses further validating the docking results, providing a theoretical basis for subsequent drug design. Tumor-derived lactate primarily originates from intracellular production by LDHA and extracellular uptake via MCT1 [44, 45], while MCT4 plays a critical role in lactate export, maintaining lactate balance [46]. Inhibiting MCT4 has been shown to significantly suppress tumor cell proliferation and migration [47]. For

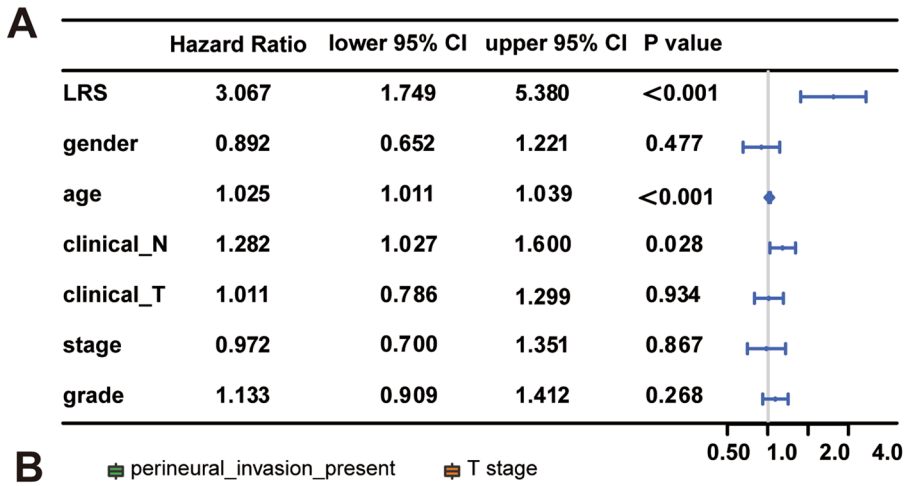
A
Hazard Ratio lower 95% CI upper 95% CI P value
LRS 3.067 1.749 5.380 <0.001
gender 0.892 0.652 1.221 0.477
age 1.025 1.011 1.039 <0.001
clinical_N 1.282 1.027 1.600 0.028
clinical_T 1.011 0.786 1.299 0.934
stage 0.972 0.700 1.351 0.867
grade 1.133 0.909 1.412 0.268
0.50 1.0 2.0 4.0

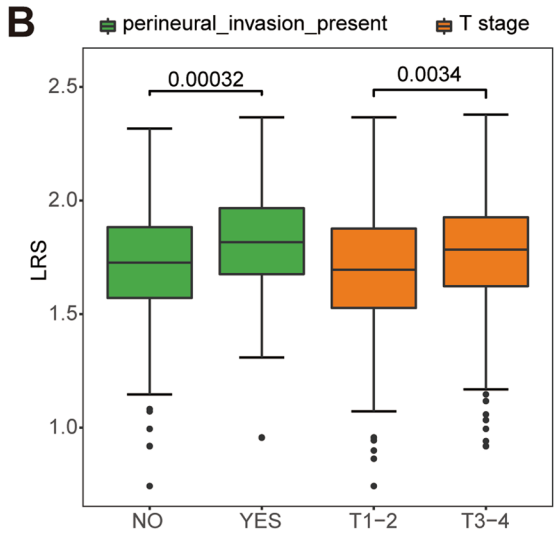
B
perineural_invasion_present
T stage
0.00032
0.0034
LRS
NO
YES
T1−2
T3−4

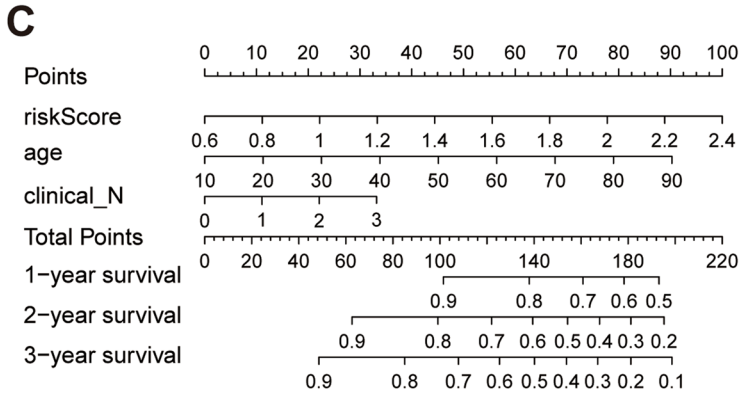
C
Points
riskScore
age
clinical_N
Total Points
1−year survival
2−year survival
3−year survival

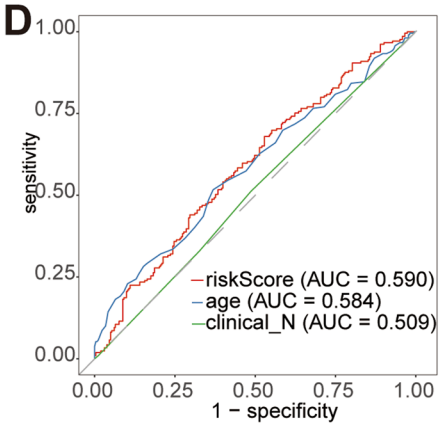
D
sensitivity
1 − specificity
riskScore (AUC = 0.590)
age (AUC = 0.584)
clinical_N (AUC = 0.509)

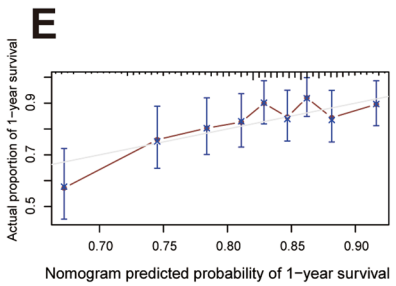
E
Actual proportion of 1−year survival
Nomogram predicted probability of 1−year survival

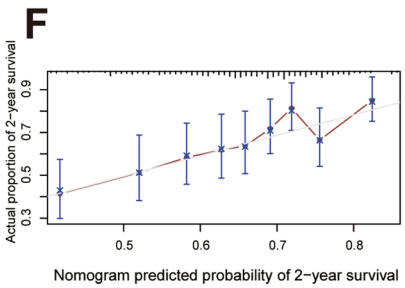
F
Actual proportion of 2−year survival
Nomogram predicted probability of 2−year survival

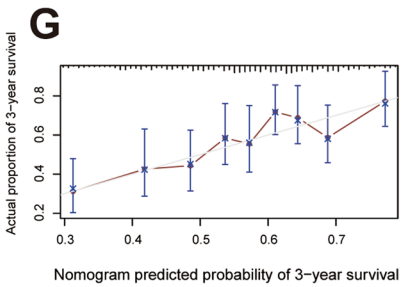
G
Actual proportion of 3−year survival
Nomogram predicted probability of 3−year survival

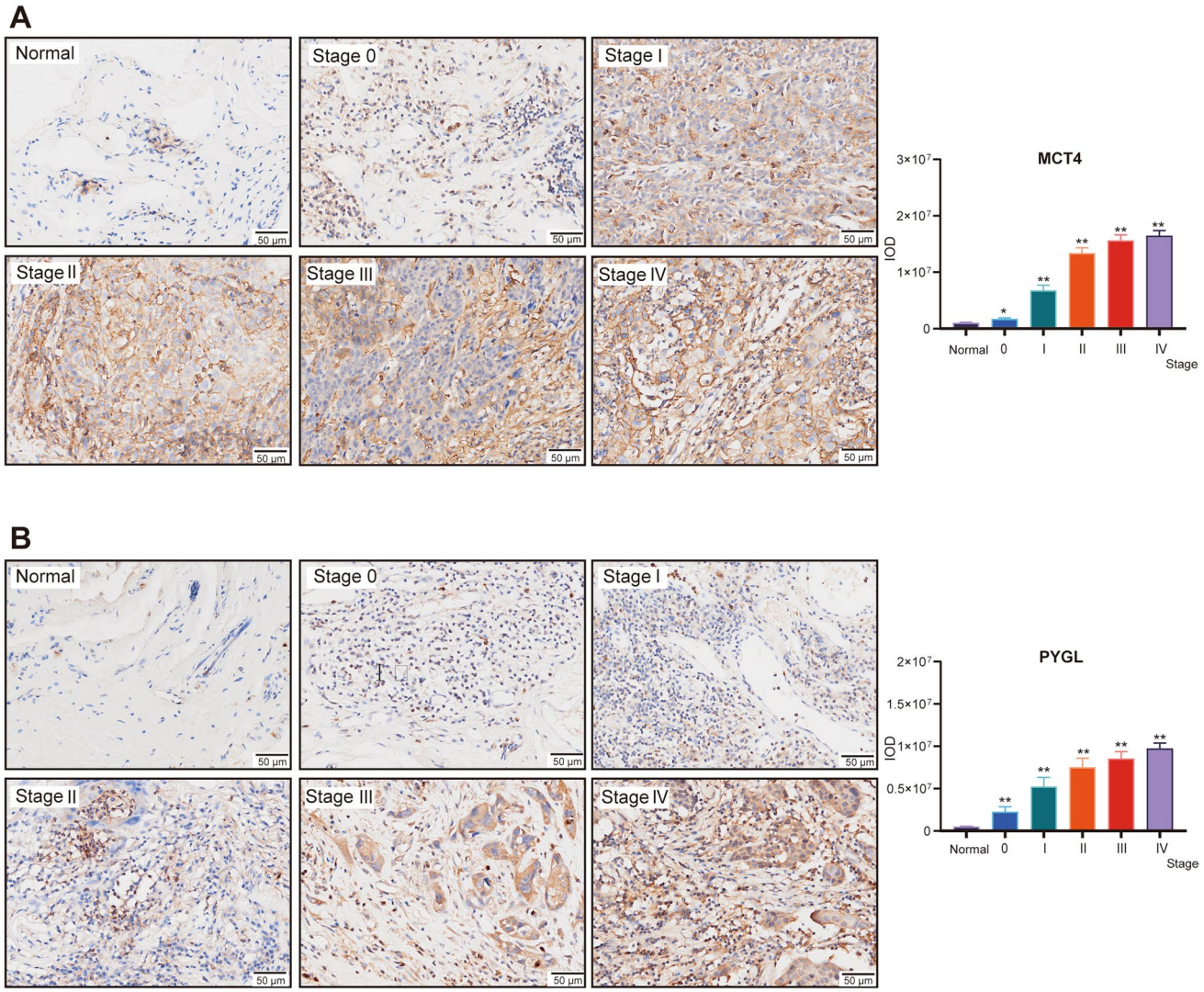

Fig. 4 Immunohistochemical expression of monocarboxylate transporter 4 (MCT4) and glycogen phosphorylase L (PYGL) in normal and tumor tissues across different clinical stages. **A** MCT4 and **B** PYGL expression progressively increase with advancing tumor stage. Data are presented as mean ± SD based on integrated optical density (IOD) measurements. *: $P < 0.05$; **: $P < 0.01$

instance, stiripentol, an antiepileptic drug, targets LDHA to block lactate production, thereby reducing DNA repair efficiency and overcoming chemoradiotherapy resistance in gastric cancer [48]. Our findings suggest that valproic acid, a well-known antiepileptic drug, stably binds to MCT4, potentially exerting anti-tumor effects or mitigating drug resistance. Previous studies support its anti-cancer potential: in breast cancer, valproic acid inhibits MCF-7 cell proliferation, induces cell cycle arrest and apoptosis, and elicits distinct responses in triple-negative breast cancer cells [49]. In gliomas, combining valproic acid with temozolomide significantly improves overall survival, particularly in younger patients [50]. Furthermore, valproic acid enhances chemotherapy efficacy in gastric cancer by modulating multidrug resistance-related gene expression [51]. Additionally, a recent study evaluated the combination of sodium valproate with the PD-L1 monoclonal antibody avelumab in HPV-associated solid tumors, including HNSCC. The results demonstrated safety and feasibility, with notable tumor regression observed in a subset of patients [52]. These findings highlight valproic acid's therapeutic versatility and underscore its potential in cancer therapy. Future research should focus on validating its efficacy in HNSCC through preclinical studies and clinical trials. Investigating its role in combination therapies and elucidating the molecular mechanisms underlying its anti-tumor effects will be critical to establishing its clinical utility in HNSCC management.

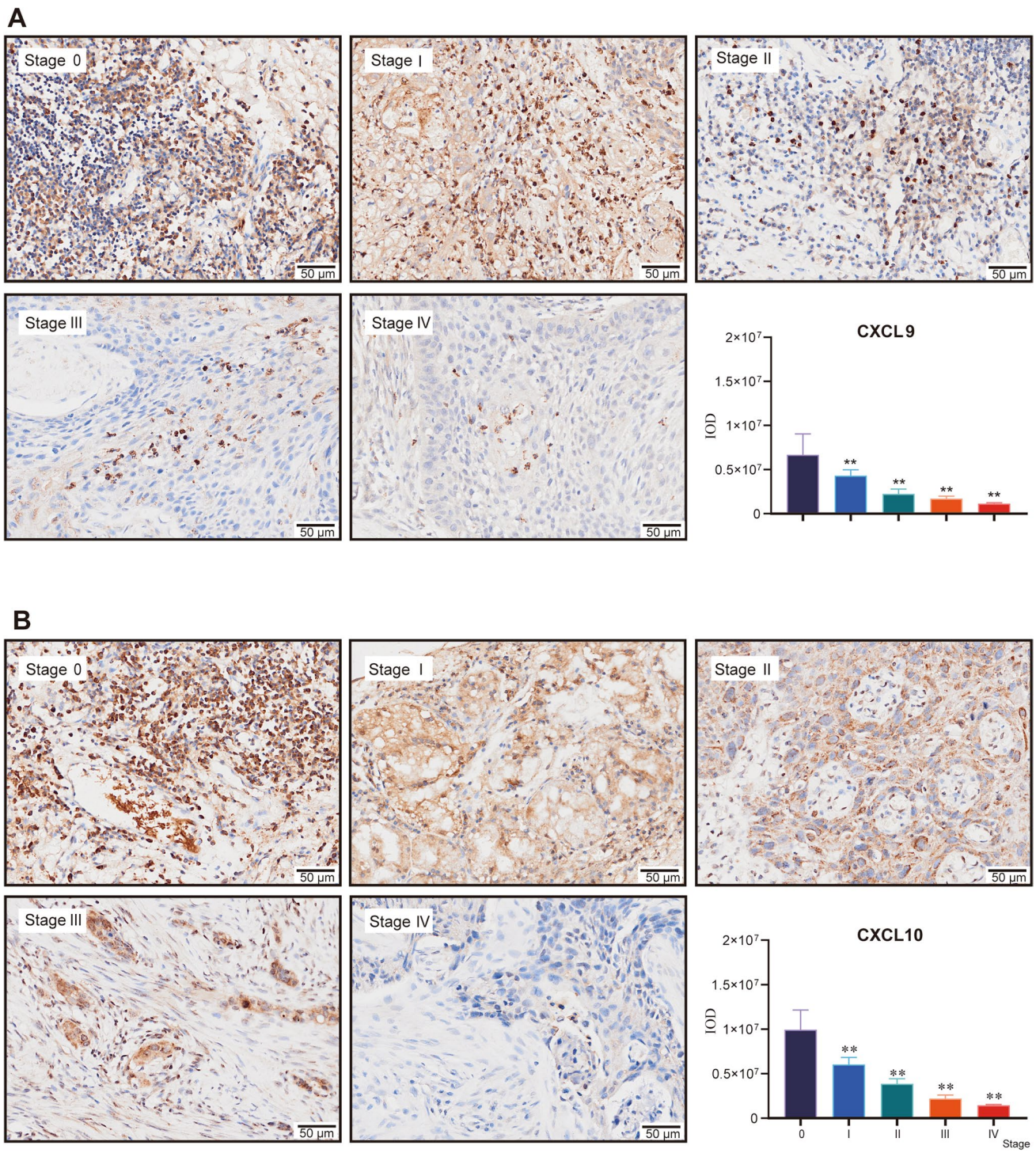

Fig. 5 Immunohistochemical expression of chemokines CXCL9 and CXCL10 in tumor tissues across different clinical stages. **A** CXCL9 and **B** CXCL10 expression progressively decrease with advancing tumor stage. Data are presented as mean ± SD based on integrated optical density (IOD) measurements. **: $P < 0.01$

5 Limitations

This study has several limitations. First, the conclusions are derived from publicly available datasets, which inherently carry sample heterogeneity and incomplete clinical annotations. Moreover, the analyses are primarily based

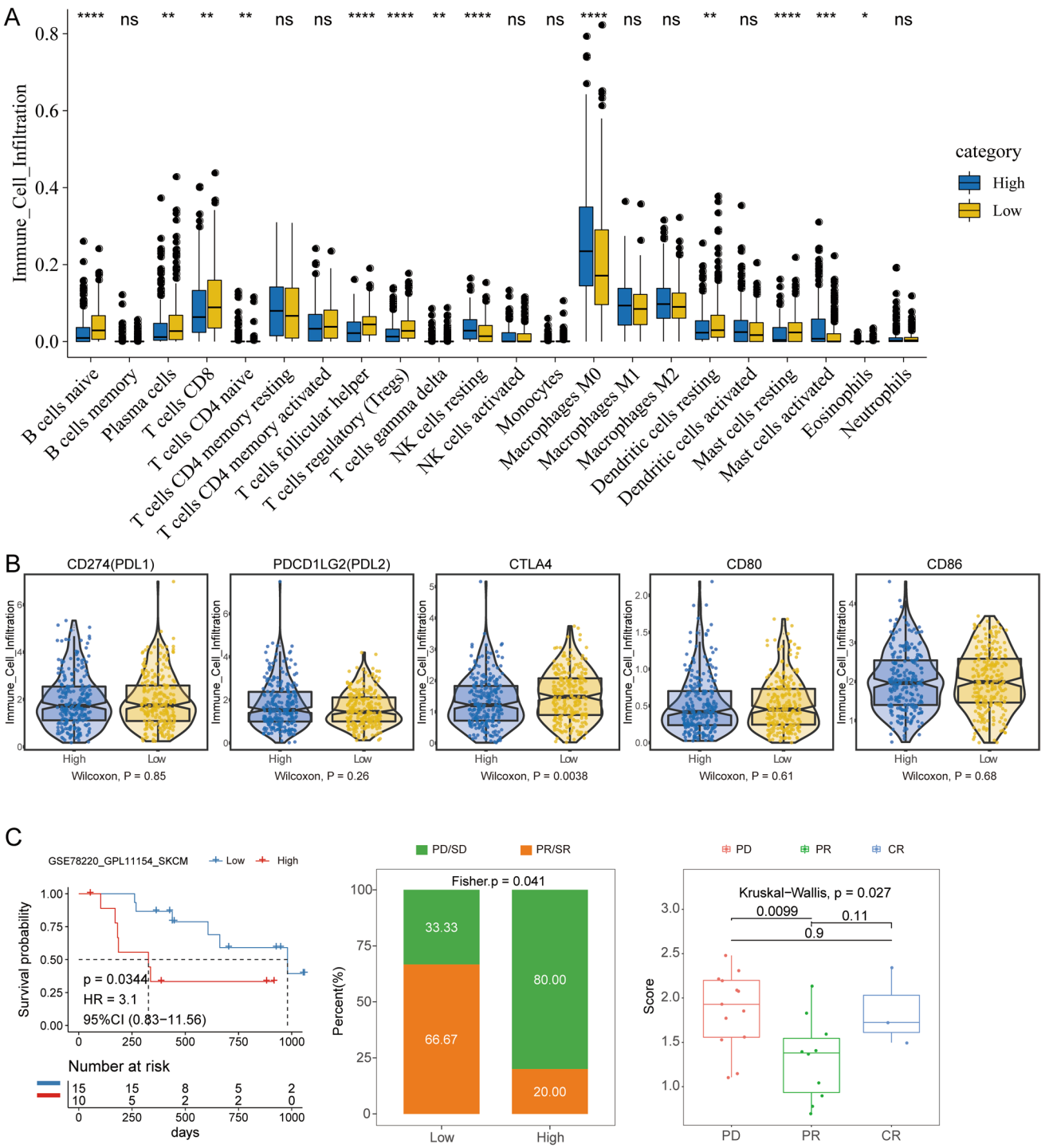

Fig. 6 Immune cell infiltration patterns, immune checkpoint expression, and immunotherapy response prediction based on the lactate-related risk score (LRS). **A** Differential infiltration of 22 tumor-infiltrating immune cell types between high- and low-risk groups, estimated using the CIBERSORTx algorithm. **B** Differential expression of immune checkpoint molecules between high- and low-risk groups. **C** Association between LRS and immunotherapy response in the GSE78220 cohort

on bioinformatic and statistical approaches, lacking experimental validation to confirm proposed mechanisms. For instance, the association between PNI and LRS remains correlative without direct mechanistic evidence. Second, although the data suggest a link between LRS and immune features within the TME, the findings are observational. Functional studies and clinical trials are required to elucidate causal relationships between lactate metabolism and

Fig. 7 Heatmap of the correlations between the lactic acid risk score and hallmark cancer pathways

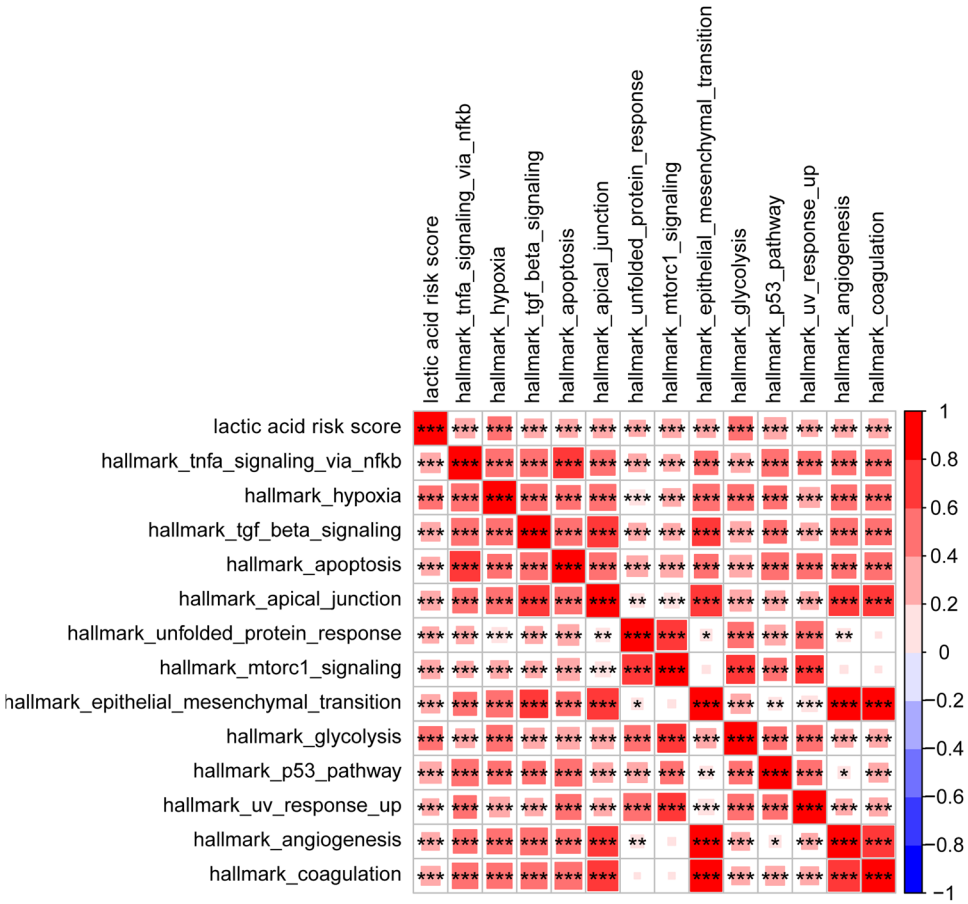

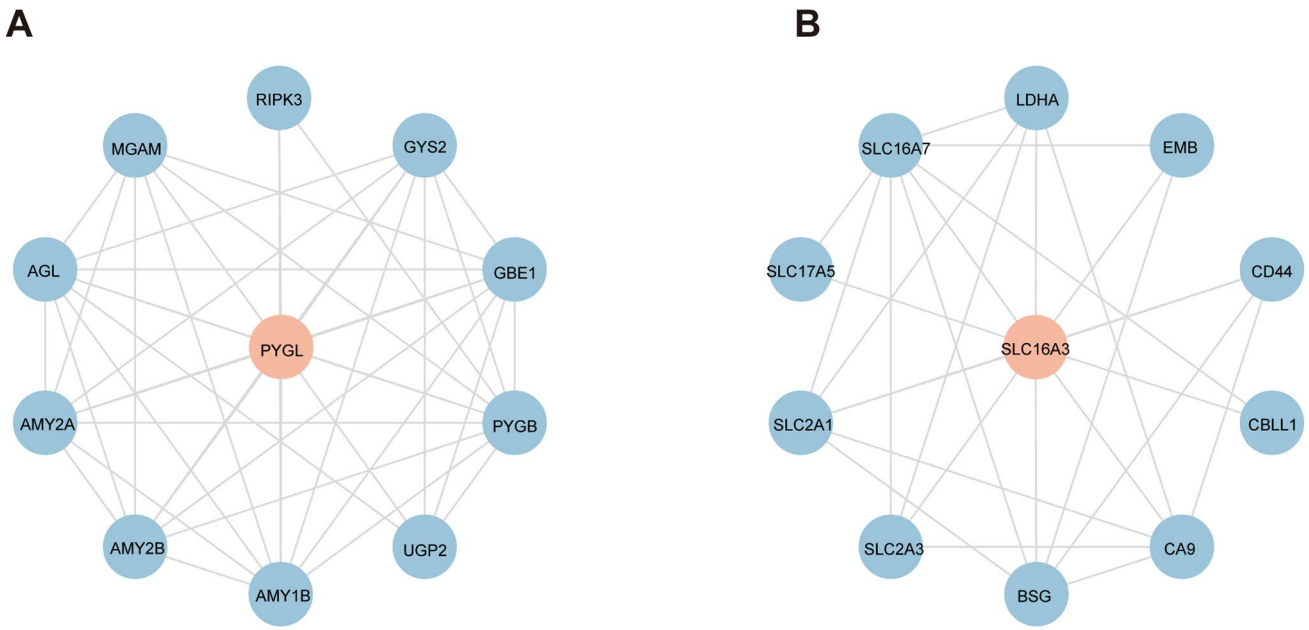

Fig. 8 Protein–protein interaction (PPI) networks for glycogen phosphorylase L (*PYGL*) and solute carrier family 16 member 3 (*SLC16 A3*). **A** PPI network for *PYGL*. **B** PPI network for *SLC16 A3*

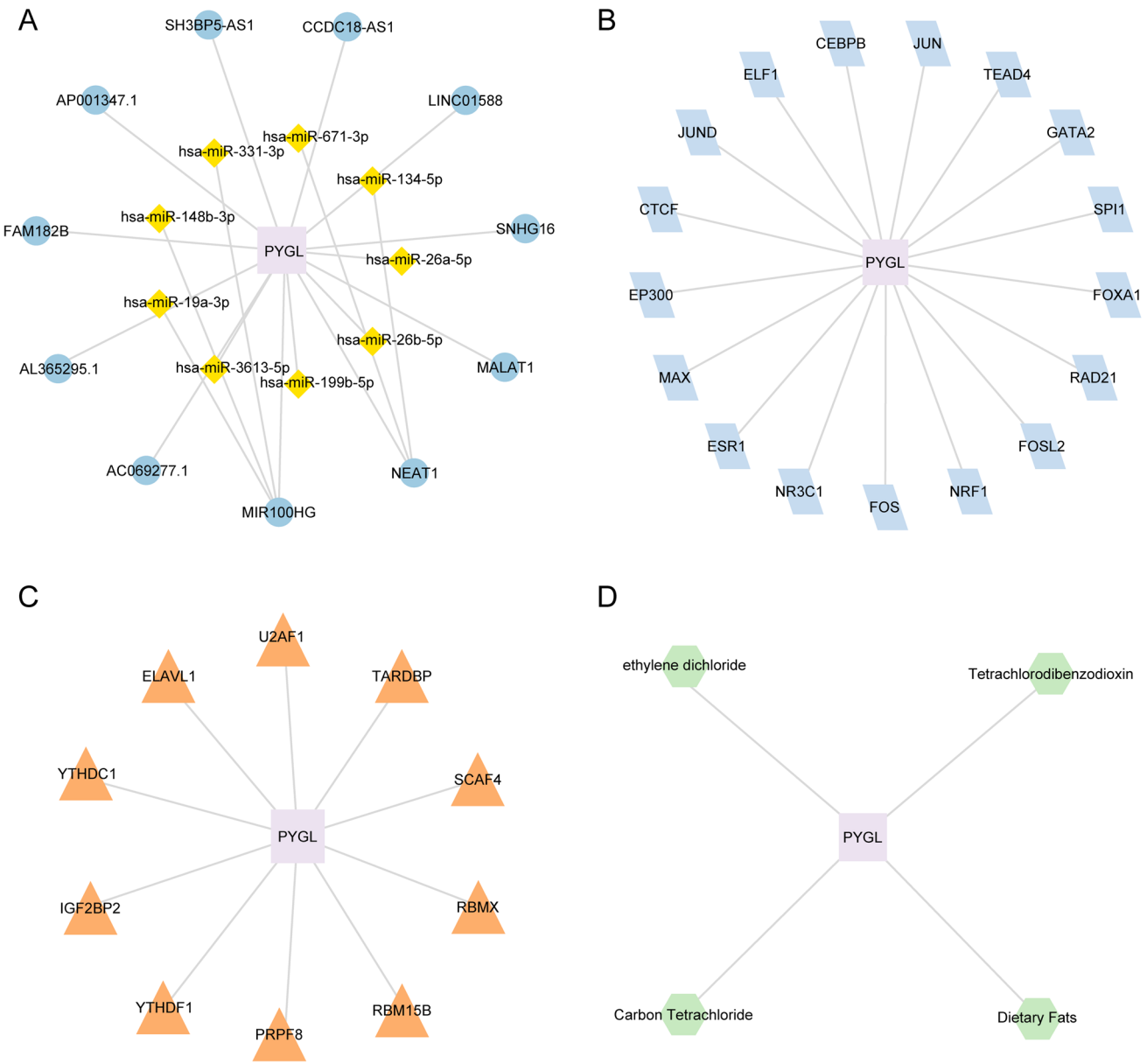

Fig. 9 Network analyses for glycogen phosphorylase L (*PYGL*). **A** ceRNA network of miRNAs and lncRNAs. **B** mRNA-TF network of transcription factors. **C** mRNA-RBP network of RNA-binding proteins. **D** mRNA-drug target interaction network of associated chemicals. *TF* transcription factor, *RBP* RNA-binding protein

immune modulation in HNSCC. In particular, the proposed role of CXCL9 and CXCL10 downregulation in immune escape requires validation in animal models. Finally, while molecular docking and dynamics simulations identify valproic acid as a potential therapeutic agent targeting MCT4, these predictions lack experimental verification. Rigorous preclinical and clinical studies are needed to assess its efficacy, safety, optimal dosing, and potential combined effect with ICIs. These limitations call for further validation through experimental and clinical studies.

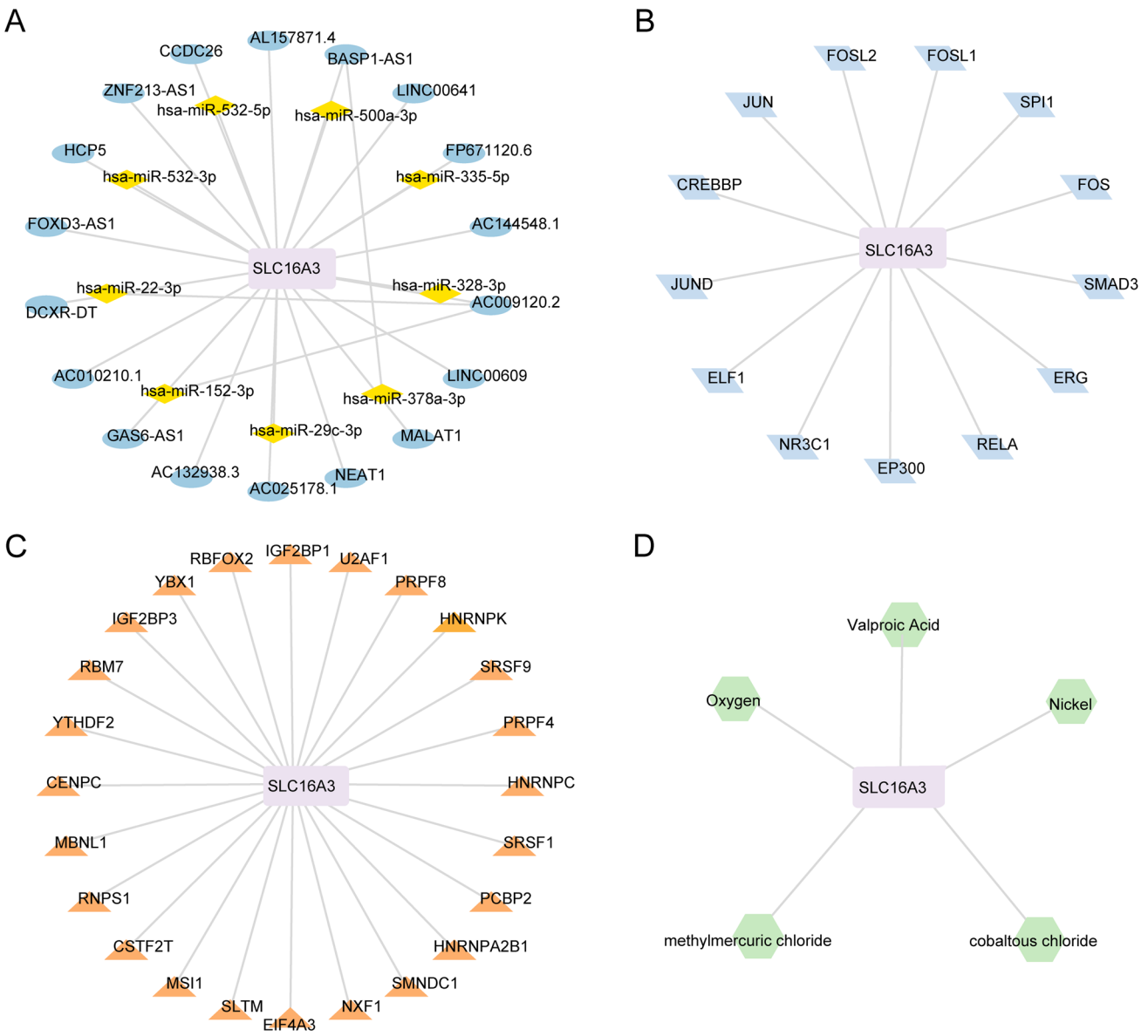

Fig. 10 Network analyses for solute carrier family 16 member 3 (*SLC16 A3*). **A** ceRNA network of miRNAs and lncRNAs. **B** mRNA-TF network of transcription factors. **C** mRNA-RBP network of RNA-binding proteins. **D** mRNA-drug target interaction network of associated chemicals. *TF* transcription factor; *RBP* RNA-binding protein

6 Conclusion

This study identified key LMGs (*SLC16 A3* and *PYGL*) in HNSCC and developed a LRS model with strong prognostic and immunotherapy predictive value. Our study demonstrates that elevated expression of PYGL and MCT4, along with reduced expression of CXCL9 and CXCL10, is closely associated with advanced tumor stage in HNSCC. This metabolic-immune expression pattern suggests a potential crosstalk between tumor metabolic reprogramming and immune suppression within the TME, highlighting PYGL and MCT4 as potential therapeutic targets to overcome immune resistance in HNSCC. Molecular docking revealed valproic acid as a potential therapeutic agent targeting *SLC16 A3*.

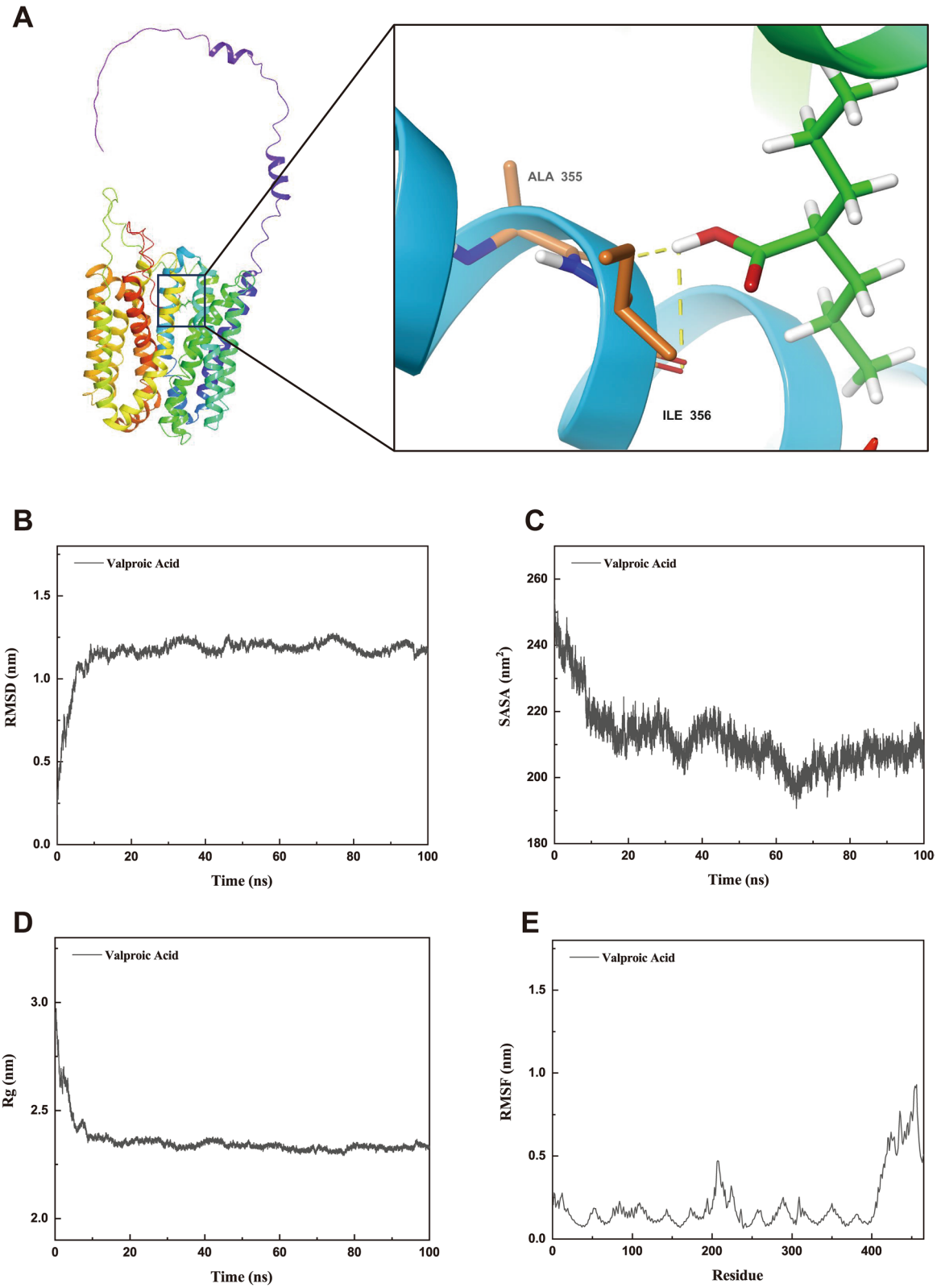

Fig. 11 Molecular Docking and Dynamics Simulation of the MCT4-Valproic Acid Complex. **A** Molecular docking analysis showing the binding energy and key hydrogen bond interactions between MCT4 and valproic acid. **B** Root Mean Square Deviation (RMSD) of the MCT4-valproic acid complex during the simulation. **C** Solvent-Accessible Surface Area (SASA) profile of the MCT4-valproic acid complex, reflecting changes in protein surface exposure. **D** Radius of Gyration (Rg) of the MCT4-valproic acid complex over time. **E** Root Mean Square Fluctuation (RMSF) of the MCT4-valproic acid complex, indicating flexibility during the simulation

Table 2 MMPBSA analysis of MCT4-valproic acid interaction

Energy (kJ/mol)	Valproic acid
van der Waals energy	– 69.261
Electrostatic energy	– 23.597
Polar solvation energy	49.895
Nonpolar solvation energy	– 14.636
Total binding energy	– 57.599
– TΔS	6.481
Total binding free energy	– 51.118

MCT4 monocarboxylate transporter 4

These findings highlight the significance of LMGs as biomarkers and therapeutic targets, providing a foundation for advancing personalized treatment in HNSCC.

Author contributions Huanyu Jiang: conceptualization, data curation, formal analysis, methodology, software, visualization, writing—original draft. Lijuan Zhou: data curation, formal analysis, resources, validation. Haidong Zhang: data curation, formal analysis, resources, validation. Shanchun Gong: data curation, formal analysis, resources, validation. Zhenkun Yu: project administration, writing—review & editing.

Funding Not applicable.

Data availability All data generated or analysed during this study are included in this published article (and its Supplementary Information files).

Declarations

Ethics approval and consent to participate The study was approved by the Ethics Committee of BenQ Medical Center affiliated with Nanjing Medical University. (Approval number: 2020041401). Informed consent (Consent to Participate and Consent to Publish) was obtained from all participants. For participants under 18, consent was obtained from a parent and/or legal guardian.

Competing interests The authors declare no competing interests.

References

1. Sung H, Ferlay J, Siegel RL, Laversanne M, Soerjomataram I, Jemal A, et al. Global Cancer Statistics 2020: GLOBOCAN estimates of incidence and mortality worldwide for 36 cancers in 185 countries. CA Cancer J Clin. 2021;71(3):209–49. https://doi.org/10.3322/caac.21660.
2. Watts F, Palme CE, Porceddu S, Sundaresan P, Clark JR, Gupta R. Clinician perspectives on the factors influencing prognostic stratification by the American Joint Commission on Cancer Head and Neck Cutaneous Squamous Cell Carcinoma Staging. Surgery. 2021;170(5):1467–73. https://doi.org/10.1016/j.surg.2021.04.019.
3. Mastronikolis NS, Delides A, Kyrodimos E, Piperigkou Z, Spyropoulou D, Giotakis E, et al. Insights into metastatic roadmap of head and neck cancer squamous cell carcinoma based on clinical, histopathological and molecular profiles. Mol Biol Rep. 2024;51(1):597. https://doi.org/10.1007/s11033-024-09476-8.
4. Boguñá N, Capdevila L, Jané-Salas E. El virus del papiloma humano y su relación con la patología de la cavidad oral. Med Clin (Barc). 2019;153(4):157–64. https://doi.org/10.1016/j.medcli.2019.02.027.
5. Takenaka Y, Uno A, Tanaka H, Takemoto N, Inohara H. Distant metastasis in head and neck squamous cell carcinoma variants: a population-based study. Head Neck. 2023;45(4):882–9. https://doi.org/10.1002/hed.27305.
6. Gao L, Zhang A, Yang F, Du W. Immunotherapeutic strategies for head and neck squamous cell carcinoma (HNSCC): current perspectives and future prospects. Vaccines (Basel). 2022;10(8):1272. https://doi.org/10.3390/vaccines10081272.

7. Tu VY, Ayari A, O'Connor RS. Beyond the lactate paradox: how lactate and acidity impact T cell therapies against cancer. Antibodies. 2021;10(3):25. https://doi.org/10.3390/antib10030025.
8. Liu X, Zhao Y, Wu X, Liu Z, Liu X. A novel strategy to fuel cancer immunotherapy: targeting glucose metabolism to remodel the tumor microenvironment. Front Oncol. 2022. https://doi.org/10.3389/fonc.2022.931104.
9. Goldman MJ, Craft B, Hastie M, Repečka K, McDade F, Kamath A, et al. Visualizing and interpreting cancer genomics data via the Xena platform. Nat Biotechnol. 2020;38(6):675–8. https://doi.org/10.1038/s41587-020-0546-8.
10. Davis S, Meltzer PS. GEOquery: a bridge between the Gene Expression Omnibus (GEO) and BioConductor. Bioinformatics. 2007;23(14):1846–7. https://doi.org/10.1093/bioinformatics/btm254.
11. Wichmann G, Rosolowski M, Krohn K, Kreuz M, Boehm A, Reiche A, et al. The role of HPV RNA transcription, immune response-related gene expression and disruptive *TP53* mutations in diagnostic and prognostic profiling of head and neck cancer. Int J Cancer. 2015;137(12):2846–57. https://doi.org/10.1002/ijc.29649.
12. Fountzilas E, Kotoula V, Angouridakis N, Karasmanis I, Wirtz RM, Eleftheraki AG, et al. Identification and validation of a multigene predictor of recurrence in primary laryngeal cancer. PLoS ONE. 2013;8(8): e70429. https://doi.org/10.1371/journal.pone.0070429.
13. Liberzon A, Birger C, Thorvaldsdóttir H, Ghandi M, Mesirov JP, Tamayo P. The molecular signatures database hallmark gene set collection. Cell Syst. 2015;1(6):417–25. https://doi.org/10.1016/j.cels.2015.12.004.
14. Mayakonda A, Lin D-C, Assenov Y, Plass C, Koeffler HP. Maftools: efficient and comprehensive analysis of somatic variants in cancer. Genome Res. 2018;28(11):1747–56. https://doi.org/10.1101/gr.239244.118.
15. Engebretsen S, Bohlin J. Statistical predictions with glmnet. Clin Epigenet. 2019;11(1):123. https://doi.org/10.1186/s13148-019-0730-1.
16. Therneau TM. Survival: survival analysis. CRAN: Contributed Packages; 2001. https://doi.org/10.32614/CRAN.package.survival
17. Newman AM, Liu CL, Green MR, Gentles AJ, Feng W, Xu Y, et al. Robust enumeration of cell subsets from tissue expression profiles. Nat Methods. 2015;12(5):453–7. https://doi.org/10.1038/nmeth.3337.
18. Hugo W, Zaretsky JM, Sun L, Song C, Moreno BH, Hu-Lieskovan S, et al. Genomic and transcriptomic features of response to anti-PD-1 therapy in metastatic melanoma. Cell. 2016;165(1):35–44. https://doi.org/10.1016/j.cell.2016.02.065.
19. Szklarczyk D, Gable AL, Lyon D, Junge A, Wyder S, Huerta-Cepas J, et al. STRING v11: protein–protein association networks with increased coverage, supporting functional discovery in genome-wide experimental datasets. Nucleic Acids Res. 2019;47(D1):D607–13. https://doi.org/10.1093/nar/gky1131.
20. Li J-H, Liu S, Zhou H, Qu L-H, Yang J-H. starBase v2.0: decoding miRNA-ceRNA, miRNA-ncRNA and protein–RNA interaction networks from large-scale CLIP-Seq data. Nucleic Acids Res. 2014;42(D1):D92–7. https://doi.org/10.1093/nar/gkt1248.
21. Huang J, Zheng W, Zhang P, Lin Q, Chen Z, Xuan J, et al. ChIPBase v3.0: the encyclopedia of transcriptional regulations of non-coding RNAs and protein-coding genes. Nucleic Acids Res. 2023;51(D1):D46–56. https://doi.org/10.1093/nar/gkac1067.
22. Davis AP, Wiegers TC, Johnson RJ, Sciaky D, Wiegers J, Mattingly CJ. Comparative toxicogenomics database (CTD): update 2023. Nucleic Acids Res. 2023;51(D1):D1257–62. https://doi.org/10.1093/nar/gkac833.
23. Shannon P, Markiel A, Ozier O, Baliga NS, Wang JT, Ramage D, et al. Cytoscape: a software environment for integrated models of biomolecular interaction networks. Genome Res. 2003;13(11):2498–504. https://doi.org/10.1101/gr.1239303.
24. Bateman A, Martin M-J, Orchard S, Magrane M, Ahmad S, Alpi E, et al. UniProt: the universal protein knowledgebase in 2023. Nucleic Acids Res. 2023;51(D1):D523–31. https://doi.org/10.1093/nar/gkac1052.
25. Kim S, Chen J, Cheng T, Gindulyte A, He J, He S, et al. PubChem 2023 update. Nucleic Acids Res. 2023;51(D1):D1373–80. https://doi.org/10.1093/nar/gkac956.
26. Wu J, Ge F, Zhu L, Liu N. Potential toxic mechanisms of neonicotinoid insecticides in rice: inhibiting auxin-mediated signal transduction. Environ Sci Technol. 2023;57(12):4852–62. https://doi.org/10.1021/acs.est.2c09352.
27. Kawata M, Nagashima U. Particle mesh Ewald method for three-dimensional systems with two-dimensional periodicity. Chem Phys Lett. 2001;340(1–2):165–72. https://doi.org/10.1016/S0009-2614(01)00393-1.
28. Darden T, York D, Pedersen L. Particle mesh Ewald: an $N\cdot\log(N)$ method for Ewald sums in large systems. J Chem Phys. 1993;98(12):10089–92. https://doi.org/10.1063/1.464397.
29. Hess B, Kutzner C, van der Spoel D, Lindahl E. GROMACS 4: algorithms for highly efficient, load-balanced, and scalable molecular simulation. J Chem Theory Comput. 2008;4(3):435–47. https://doi.org/10.1021/ct700301q.
30. Carretero-González R, Kevrekidis PG, Kevrekidis IG, Maroudas D, Frantzeskakis DJ. A Parrinello-Rahman approach to vortex lattices. Phys Lett A. 2005;341(1–4):128–34. https://doi.org/10.1016/j.physleta.2005.04.046.
31. Zhang F, Liu Y, Yang Y, Yang K. Development and validation of a fourteen- innate immunity-related gene pairs signature for predicting prognosis head and neck squamous cell carcinoma. BMC Cancer. 2020;20(1):1015. https://doi.org/10.1186/s12885-020-07489-7.
32. Tian G, Zhang J, Bao Y, Li Q, Hou J. A prognostic model based on Scissor+ cancer associated fibroblasts identified from bulk and single cell RNA sequencing data in head and neck squamous cell carcinoma. Cell Signal. 2024;114: 110984. https://doi.org/10.1016/j.cellsig.2023.110984.
33. Li X, Wang Y, Zhai Z, Mao Q, Chen D, Xiao L, et al. Predicting response to immunotherapy in gastric cancer via assessing perineural invasion-mediated inflammation in tumor microenvironment. J Exp Clin Cancer Res. 2023;42(1):206. https://doi.org/10.1186/s13046-023-02730-0.
34. Chen Z, Fang Y, Jiang W. Important cells and factors from tumor microenvironment participated in perineural invasion. Cancers (Basel). 2023;15(5):1360. https://doi.org/10.3390/cancers15051360.
35. Cao Y, Yi Y, Han C, Shi B. NF-κB signaling pathway in tumor microenvironment. Front Immunol. 2024. https://doi.org/10.3389/fimmu.2024.1476030.
36. Yang Y, Luo N, Gong Z, Zhou W, Ku Y, Chen Y. Lactate and lysine lactylation of histone regulate transcription in cancer. Heliyon. 2024;10(21): e38426. https://doi.org/10.1016/j.heliyon.2024.e38426.
37. Tzorakoleftheraki S-E, Koletsa T. The complex role of mast cells in head and neck squamous cell carcinoma: a systematic review. Medicina (B Aires). 2024;60(7):1173. https://doi.org/10.3390/medicina60071173.
38. Zhang Y, Rao Y, Lu J, Wang J, Ker DFE, Zhou J, et al. The influence of biophysical niche on tumor-associated macrophages in liver cancer. Hepatol Commun. 2024. https://doi.org/10.1097/HC9.0000000000000569.

39. Liu S, Zhang X, Wang W, Li X, Sun X, Zhao Y, et al. Metabolic reprogramming and therapeutic resistance in primary and metastatic breast cancer. Mol Cancer. 2024;23(1):261. https://doi.org/10.1186/s12943-024-02165-x.
40. Huang Y, Liu H, Liu X, Li N, Bai H, Guo C, et al. The chemokines initiating and maintaining immune hot phenotype are prognostic in ICB of HNSCC. Front Genet. 2022. https://doi.org/10.3389/fgene.2022.820065.
41. Zhang A, Fan T, Liu Y, Yu G, Li C, Jiang Z. Regulatory T cells in immune checkpoint blockade antitumor therapy. Mol Cancer. 2024;23(1):251. https://doi.org/10.1186/s12943-024-02156-y.
42. Nathan C, Khandelwal AR, Wolf GT, Rodrigo JP, Mäkitie AA, Saba NF, et al. *TP53* mutations in head and neck cancer. Mol Carcinog. 2022;61(4):385–91. https://doi.org/10.1002/mc.23385.
43. Lin X, Zhou W, Liu Z, Cao W, Lin C. Targeting cellular metabolism in head and neck cancer precision medicine era: a promising strategy to overcome therapy resistance. Oral Dis. 2023;29(8):3101–20. https://doi.org/10.1111/odi.14411.
44. Ippolito L, Morandi A, Giannoni E, Chiarugi P. Lactate: a metabolic driver in the tumour landscape. Trends Biochem Sci. 2019;44(2):153–66. https://doi.org/10.1016/j.tibs.2018.10.011.
45. Rabinowitz JD, Enerbäck S. Lactate: the ugly duckling of energy metabolism. Nat Metab. 2020;2(7):566–71. https://doi.org/10.1038/s42255-020-0243-4.
46. Payen VL, Mina E, Van Hée VF, Porporato PE, Sonveaux P. Monocarboxylate transporters in cancer. Mol Metab. 2020;33:48–66. https://doi.org/10.1016/j.molmet.2019.07.006.
47. Zhang H, Wang Z, Gao T, Wang Z, Ren C, Liu J. An enzyme-instructed self-assembly system induces tumor acidosis via sequential-dual effect for cancer selective therapy. Acta Biomater. 2023;164:447–57. https://doi.org/10.1016/j.actbio.2023.03.036.
48. Chen H, Li Y, Li H, Chen X, Fu H, Mao D, et al. NBS1 lactylation is required for efficient DNA repair and chemotherapy resistance. Nature. 2024;631(8021):663–9. https://doi.org/10.1038/s41586-024-07620-9.
49. Giordano F, Paolì A, Forastiero M, Marsico S, De Amicis F, Marrelli M, et al. Valproic acid inhibits cell growth in both MCF-7 and MDA-MB231 cells by triggering different responses in a cell type-specific manner. J Transl Med. 2023;21(1):165. https://doi.org/10.1186/s12967-023-04015-8.
50. Kuo Y-J, Yang Y-H, Lee I-Y, Chen P-C, Yang J-T, Wang T-C, et al. Effect of valproic acid on overall survival in patients with high-grade gliomas undergoing temozolomide. Medicine. 2020;99(28): e21147. https://doi.org/10.1097/MD.0000000000021147.
51. Hosseini SA, Mirzaei SA, Kermani S, Yaghoobi H. Valproate modulates the activity of multidrug resistance efflux pumps, as a chemoresistance factor in gastric cancer cells. Mol Biol Rep. 2024;51(1):427. https://doi.org/10.1007/s11033-024-09284-0.
52. Bozorgmehr N, Syed H, Mashhouri S, Walker J, Elahi S. Transcriptomic profiling of peripheral blood cells in HPV-associated carcinoma patients receiving combined valproic acid and avelumab. Mol Oncol. 2024;18(5):1209–30. https://doi.org/10.1002/1878-0261.13519.